Featured in Physics

Magnetic levitation by rotation

Joachim Marco Hermansen,[1,†] Frederik Laust Durhuus,[2,†] Cathrine Frandsen,[2]
Marco Beleggia,[3,4] Christian R.H. Bahl,[1] and Rasmus Bjørk[1,*]

[1]*Department of Energy Conversion and Storage, Technical University of Denmark (DTU), Kongens Lyngby DK-2800, Denmark*
[2]*Department of Physics, Technical University of Denmark (DTU), Kongens Lyngby DK-2800, Denmark*
[3]*DTU Nanolab, Technical University of Denmark (DTU), Kongens Lyngby DK-2800, Denmark*
[4]*Department of Physics, Informatics and Mathematics, University of Modena and Reggio Emilia, Modena 40125, Italy*

A permanent magnet can be levitated simply by placing it in the vicinity of another permanent magnet that rotates in the order of 200 Hz. This surprising effect can be easily reproduced in the laboratory with off-the-shelf components. Here, we have investigated this novel type of magnetic levitation experimentally and clarified the underlying physics. Using a 19-mm-diameter spherical Nd-Fe-B magnet as the rotor magnet, we have captured the detailed motion of levitating spherical Nd-Fe-B magnets, denoted floater magnets, as well as the influence of the rotation speed and magnet size on the levitation. We have found that as levitation occurs, the floater-magnet frequency locks with the rotor magnet and, noticeably, that the magnetization of the floater is oriented close to the axis of rotation and toward the like pole of the rotor magnet. This is in contrast to what might be expected by the laws of magnetostatics, as the floater is observed to align its magnetization essentially perpendicular to the magnetic field of the rotor. Moreover, we have found that the size of the floater has a clear influence on the levitation: the smaller the floater, the higher the rotor speed that is necessary to achieve levitation and the further away the levitation point shifts. Despite the unexpected magnetic configuration during levitation, we have verified that magnetostatic interactions between the rotating magnets are responsible for creating the equilibrium position of the floater. Hence, this type of magnetic levitation does not rely on gravity as a balancing force to achieve an equilibrium position. Based on theoretical arguments and a numerical model, we show that a constant vertical field and eddy-current-enhanced damping are sufficient to produce levitation from rest. This enables a gyroscopically stabilized counterintuitive steady-state moment orientation and the resulting magnetostatically stable midair equilibrium point. The numerical model displays the same trends with respect to the rotation speed and the floater-magnet size as seen in the experiments.

I. INTRODUCTION

Magnetic levitation is equally science fiction and present-day technology. Since Earnshaw's theorem prevents stable levitation with systems comprising only ferromagnets, current technologies such as Maglev trains [1], flywheels [2], and high-speed machinery [3] rely on different physical compensation techniques to achieve levitation.

A novel type of magnetic levitation has recently been discovered [4] that uses two permanent magnets of similar size. One magnet, termed the "rotor," mounted on a motor with its north and south poles oriented perpendicular to the rotation axis, is brought to rotate at angular velocities in

the order of 10, 000 rpm. The second magnet, termed the "floater," is placed in the vicinity of the rotating magnet: it is spun in motion and it levitates toward the rotor until it floats in space a few centimeters below it. The floater precesses with the same frequency as the rotor and, if perturbed, experiences restoring forces that bring it back to its equilibrium position. It is quite surprising that magnetic levitation develops in such a relatively simple system: the magnetic forces do not suddenly create a stable minimum-energy point in space just by spinning one of the magnets and yet levitation can be very easily reproduced in the laboratory with off-the-shelf components, as shown in Video 1 or at Ref. [5].

Ferromagnetic levitation can generally be subdivided into three categories to counteract gravity. The first is active magnetic stabilization, where a control system supplies the levitating magnet with an electromagnetic

*rabj@dtu.dk
†These authors contributed equally to this work.
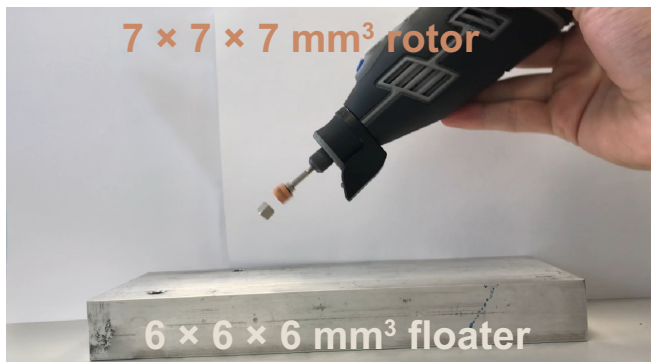
VIDEO 1.   A demonstration of an easily reproducible experiment using a Dremel multitool to achieve magnetic levitation.

force to keep it balanced [3,6,7]. The second type is electrodynamic suspension, known from Maglev trains, where a moving magnet will induce a current in a stationary conductor, producing a repulsive force that increases with the speed of the moving magnet [1]. Finally, the last category is spin-stabilized levitation, where the levitating object is spinning and uses the gyroscopic effect to keep the system stable. This is the effect seen in the Levitron™ [8,9] and the magnetic Paul trap [10,11].

The spinning rate of the Levitron is typically 500 rpm [12], much lower than seen in the novel type of magnetic levitation. Furthermore, since it is not a driven system, once friction with the air slows the magnet spinning rate, it loses levitation. The magnetic Paul trap uses a rotating gradient field for levitation and hence is driven; however, it relies on a balance between gravity and magnetic repulsion for vertical stability. For the levitation studied in this paper, both attraction and repulsion are magnetic, so the floater magnet is fixed relative to the rotor even when moving and rotating the whole device. Thus the phenomenon can be used for the trapping and three-dimensional (3D) contactless manipulation of magnetic objects, similar to how Refs. [13–15] have used spinning dipole magnets for handling metal spheres. Reference [13] relies on eddy currents for inducing a coupling and complex feedback control for stability. For the levitation presented here, eddy currents are relevant but not required for levitation and the phenomenon is inherently stable. Determining the full range of applications requires a deeper understanding of the present phenomenon; in particular, the scalability and range of stability for levitation, but other potential applications could include trapping and manipulating of ferromagnetic microparticles.

In the recent pioneering work [4], Ucar explains the novel magnetic levitation in terms of two key concepts: polarity-free magnetic repulsion (PFR) and the magnetic bound state (MBS). PFR is a short-range repulsive force with $F \propto \frac{1}{r^7}$ decay with distance that is postulated to originate from the synchronization of the floater magnet and

the rotor magnet. It is assumed that the rotor and floater will have a constant phase relative to each other and from that assumption the repelling force emerges. However, this assumption is not clearly validated in the work. MBS is the stable levitation that can occur if the rotor magnet is tilted and/or shifted with respect to the rotation axis, as this in combination with the tilt of the floater magnet can result in an attractive force with a stable equilibrium point. However, this is not rigorously and systematically investigated in Ucar's work.

The pioneering paper by Ucar and a short follow-up manuscript comparing the system to a Kapitza pendulum [16] do not decipher many key aspects of the levitation mechanism. There is no discussion about how stable the magnetic levitation phenomenon is and what kinds of instabilities can cause levitation to cease, or about when these occur. Furthermore, the influence of the rotor speed, the floater size, and the floater magnetization on levitation is not discussed. The detailed orientation of the floater relative to the rotor is also not quantified experimentally. Furthermore, on the theoretical side, Ucar has exclusively considered energy-conserving models of magnetostatic coupling and an analysis of eddy currents and the effect of drag is not considered. A systematic study of how the various parameters influence the levitation is crucial to understanding the physics behind this novel levitation effect. In this paper, we have considered these aspects experimentally using high-speed video tracking. We then discuss the various physical effects in the system and their relevance. Finally, we simulate a simple dynamical model of the system to elucidate the mechanisms behind levitation.

II. EXPERIMENTAL SETUP

We have realized an experimental setup as follows. A spherical Nd-Fe-B rotor magnet with a diameter of 19 mm and a nominal remanence of 1.22–1.26 T was fixed using epoxy into a 3D-printed plastic holder. The rotor orientation was specified and determined by placing a neodymium magnet on the side of the 3D-printed rotor mount, such that the magnetization direction was kept aligned while the epoxy cured. The holder was subsequently mounted onto the shaft of a high-speed motor (Vevor JST-JGF-F65A) with speed control, assembled on an aluminum support. The motor allows for experiments at rotational speeds up to 400 Hz or 24,000 rpm, calibrated using an induction coil and oscilloscope setup. This is comparable to the work of Ucar, who uses rotor speeds between 5530 rpm and 105,000 rpm [4]. The intrinsic alternating magnetic field of the motor at a typical distance of the floater magnet is assumed to be negligible. The experimental setup is shown in Fig. 1.

After epoxying the rotor magnet onto its holder, all three spatial components of the magnetic field produced by the
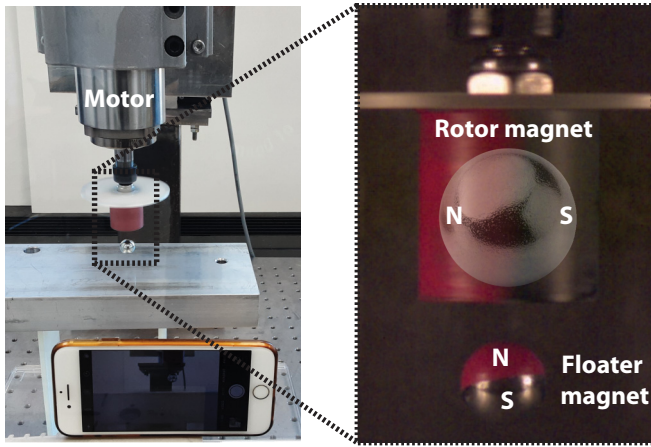
FIG. 1. The experimental setup, including a closeup of the rotor and floater magnet. The closeup is an image taken with the high-speed camera and where the floater magnet has been painted to indicate its magnetic poles. The floater magnet can clearly be seen to be levitating.

rotor magnet were measured by a Hall probe in 361 positions in a 190 mm by 190 mm slice 155 mm above the center of the rotor magnet. Fitting the measured field with a dipolar field resulted in a polar angle $\theta_r = 90.5° \pm 2.5°$ (cf. Fig. 2) i.e., close to the desired direction.

During experiments, the dynamical behavior of the floater magnet was filmed and the recordings postprocessed with the motion-tracking software TRACKER to determine the position and orientation of the floater as a function of time, as demonstrated in Video 2. Two different camera setups were used. The low-speed option consisted of an iPhone 7 camera recording at 30 frames/s. For faster dynamics, a Chronos 1.4 high-speed camera recording at 1057 frames/s was used.

To consistently reproduce and test the magnetic levitation phenomenon, we have adopted the following experimental protocol. First, the motor was spun at the desired speed with a 30-mm-thick aluminum plate placed 35 mm below the rotor magnet. The purpose of the aluminum plate was to dampen the initial transient motion of the floater through eddy currents, allowing for an easier initial levitation. After being inserted manually beneath the rotor, the floater magnet quickly levitated toward its equilibrium position. As soon as this was reached, the aluminum plate was removed and it was thus only present during the initial levitation of the floater magnet. We note that with practice the floater magnet can be levitated without the aluminum plate. The procedure described above is shown in a video recording in Video 3 or at Ref. [5].

III. RESULTS

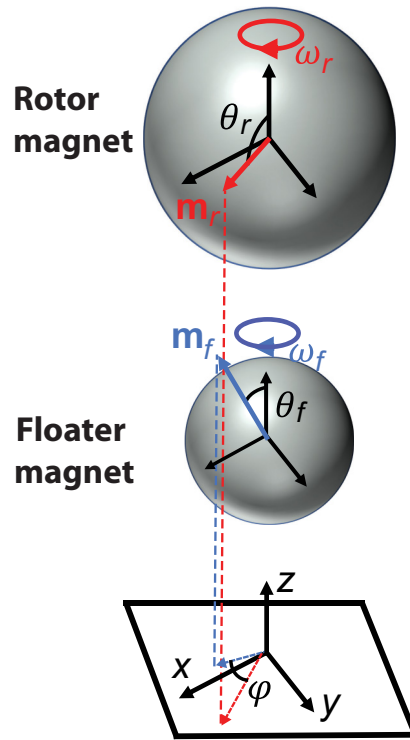The magnetic levitation was investigated by three different experiments. The first was aimed at understanding the

FIG. 2. The phase angle, φ, between the floater and the rotor magnets. The phase angle is the angle between the projection onto the x-y plane of the respective magnetization vectors of the two magnets, $\mathbf{m}_r$ and $\mathbf{m}_f$. The levitation distance is the center-to-center distance between the rotor and the floater magnets.

detailed alignment of the rotor and floater magnets for a fixed set of experimental parameters. The second focused on the dynamics of the floater magnet as a function of the rotor speed for a fixed-size floater. The third experiment investigated the role of the rotor size and magnetization on levitation.
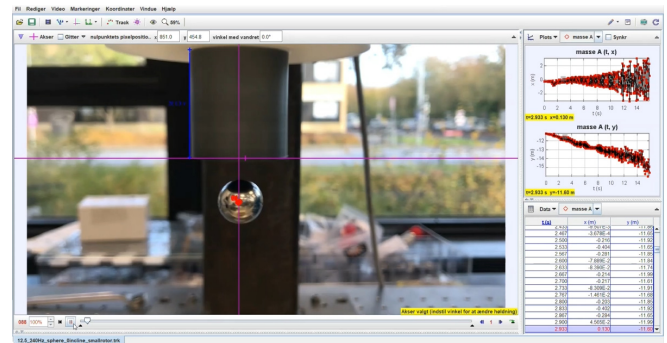
VIDEO 2. A demonstration of the motion-tracking software TRACKER used to determine the position and orientation of the floater as a function of time.
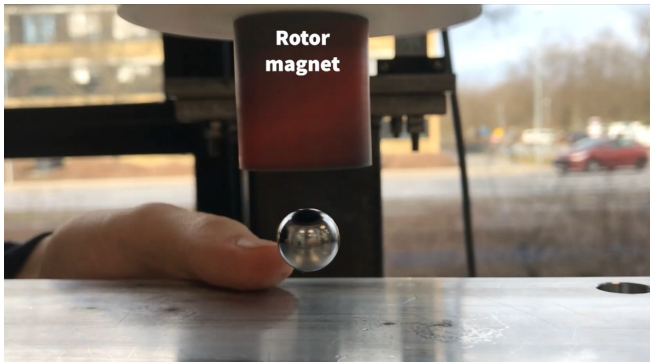
VIDEO 3.   The procedure to reproduce the magnetic levitation phenomenon.

A. Floater alignment

First, we established the exact movement of the floater magnet. It is particularly important to determine the orientation of the floater magnet, i.e., the direction of its magnetization during rotation. To establish the polar angle of the floater magnet, θ_f, as well as the phase angle, φ, between the rotor and floater magnetization vectors in the x-y plane (cf. Fig. 2), an experiment was performed with a spherical Nd-Fe-B floater magnet with a diameter of 12.7 mm and a remanence of 1290–1320 mT, with the rotor magnet rotating at 200 Hz. The rotor magnet was painted red on its magnetic northern hemisphere and the floater magnet was painted red on its north-pole side, to allow their orientations to be tracked. The details showing the tracking method can be found in the Supplemental Material [18] and an example experimental video is shown in Video 4. Noticeably, the polar angle is determined to be $\theta_f = 7° \pm 4°$ and the phase angle $\varphi = 6.4° \pm 5.1°$. This configuration (seen in Fig. 1) is surprising from a purely magnetostatic point of view, as the magnetization of the floater magnet is almost vertical and makes a north-north orientation with the rotor magnet, i.e., it points essentially perpendicular to the magnetic field of the rotor magnet. We stress that the orientation of the magnetization vectors shown in Fig. 2 is equally likely to be north-north as south-south.

B. Floater dynamics

To establish the floater-movement dynamics, a series of experiments using the 12.7-mm-diameter spherical Nd-Fe-B floater magnet with a remanence of 1290–1320 mT was conducted. The rotor speed was varied in steps of 5 Hz from 130 Hz to 280 Hz, with an additional measurement at 142.5 Hz, as it was the lowest speed for which levitation was possible. Depending on the dynamics, between two and five experiments were done for each rotor speed.

For each experiment, the dynamics of the floater magnet were tracked using the low-speed video setup. The
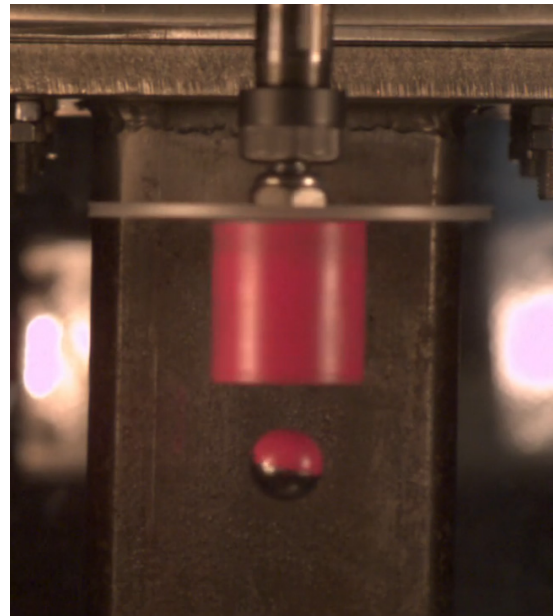

VIDEO 4.   High-speed camera footage at 1057 frames/s of the painted magnet levitating. The rotor magnet is rotating at 200 Hz.

recorded videos reveal one semistable behavior and four different types of vibrational modes of the floater magnet, as a function of the frequency of the rotor magnet. The semistable behavior is characterized by rotation during levitation without additional oscillation modes, i.e., displacement amplitudes of < 1 mm on time scales shorter than 0.5 s. The four vibrational modes are an up-down mode with oscillations up to 4 mm, defined by vertical oscillations of the floater magnet, a side mode with oscillations up to 8 mm, where the floater magnet oscillations are in the horizontal plane and swing out in a horizontal circular path around the origin, a mixed mode with oscillations up to 3.5 mm and 7 mm for the up-down mode and side modes, respectively, and a U-shaped mode with oscillations up to 7.5 mm, where the floater oscillations have a clear U shape. Each of these modes is illustrated in Videos 5, 6, 7, 8, and 9 or at Ref. [5].

In all experiments, the levitation was unstable and eventually the floater magnet dropped away from the rotor magnet, if the motion of the floater was not damped by an eddy current generated in, e.g., an aluminum plate below the floater.

From the tracked data, the levitation time and the initial levitation distance were measured [Fig. 3(a) and 3(b), respectively]. In Fig. 3(a), it can be seen that the dynamics of the system are highly dependent on the rotor speed. Below 142.5 Hz, no levitation was observed. At low speeds between 142.5 Hz and 180 Hz, no vibrational modes were present and the floater magnet descended slowly until finally dropping. At a rotor speed of 185 Hz, the dynamics changed suddenly and an up-down motion
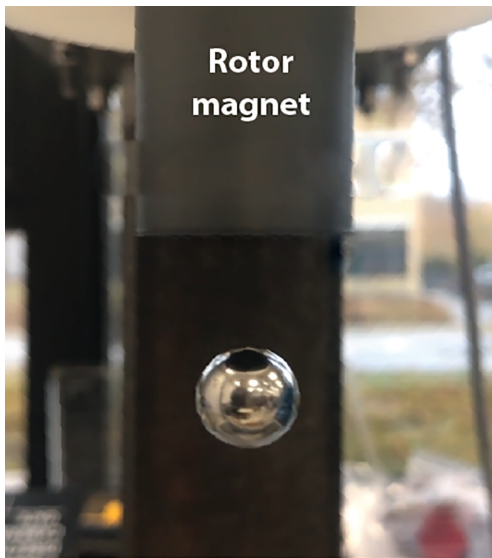
VIDEO 5.   The semistable movement mode.
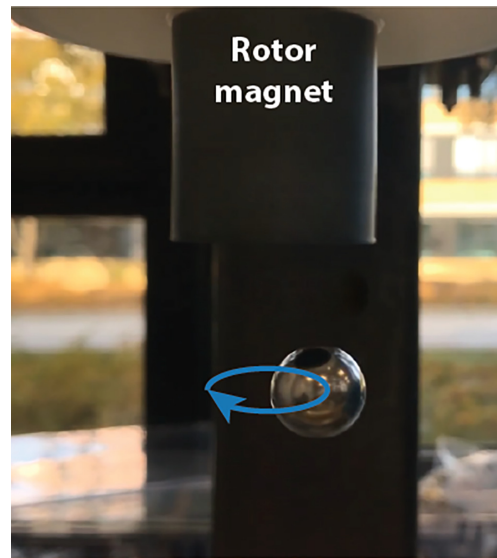
VIDEO 7.   The side movement mode.

was present, which grew with time, resulting in increased instability and a resulting decrease in the levitation time. At 195 Hz, the dynamics changed once again and the side mode appeared. With this mode, a sudden increase in levitation time was observed. Increasing the rotor speed further resulted in a rapid drop in the levitation time. At 215 Hz, a new mode appeared, with complex dynamics. The floater motion here was a mix of the side and up-down modes. Finally, at even higher speeds, the U-shaped mode appeared. The highest speed at which the levitation could occur was 280 Hz; beyond that speed, the rotor and floater magnets collided and the floater magnet was flung off.

Regarding the initial levitation distance, shown in Fig. 3(b), it is clear that regardless of the vibrational mode, the initial levitation distance becomes shorter at higher rotor speeds. This clearly shows that the force between the two magnets changes with the rotation speed. Note that it is the initial levitation distance that is shown. For all rotor speeds for this size of floater magnet, the levitation is unstable, unless, e.g., an aluminum plate is used to dampen the motion and thus the levitation distance increases over time. If we specifically consider the semistable regime where no oscillating modes are present, the fall rate can be investigated in more detail. Here, for each experiment between 142.5 Hz and 180 Hz, a linear curve was fitted to
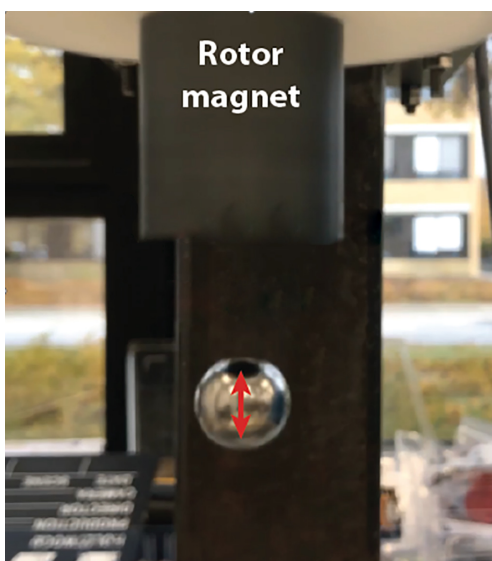
VIDEO 6.   The up-down movement mode.
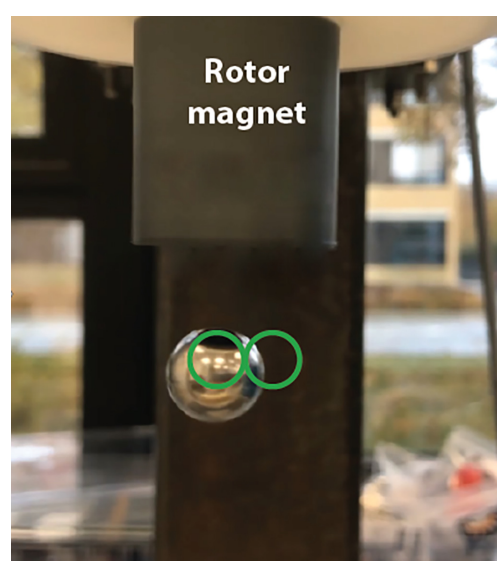
VIDEO 8.   The mixed movement mode.
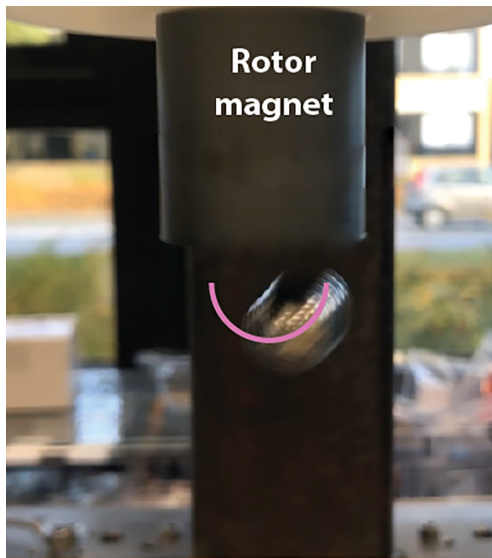
VIDEO 9. The U-shaped movement mode.

the dynamics of the floater, to find the fall rate. The time dynamics are available in the data repository at Ref. [17] and the determined fall rates are shown in Fig. 4. As can be seen, the fall rate decreases with increased rotor speed.

C. Floater magnetization and size

It is also of interest to investigate the influence of the floater size and magnetization on the rotation dynamics. The floater size was changed by using differently sized floater magnets. These magnets had a slightly varying magnetization, with the 5 and the 12.7 mm spheres having a remanence of 1290–1320 mT, the 6, 8, 19, and 26 mm spheres having a remanence of 1220–1260 mT, and the 10 and 30 mm spheres having a remanence of 1260–1290 mT. The weights of the spheres were as follows: the 5 mm sphere weighs 0.5 g, the 6 mm 0.86 g, the 8 mm 2 g, the 10 mm 4 g, the 12.7 mm 8.2 g, the 19 mm 27 g, the 26 mm 70 g, and the 30 mm 110 g.

To vary the remanence, heating was used to reduce the magnetization of six spherical magnets with diameters of 12.7 mm. The magnets were heated in an oven for 1 h each, at temperatures varying from 150°C to 200°C with 10°C intervals, in order to gradually demagnetize them [19]. Along with each spherical magnet, a cube magnet of size $7 \times 7 \times 7$ mm³ and with the same remanence was placed in the oven. Following heat treatment, the magnetization of the cube magnet was measured on a Brockhaus Hystograph HG 200, which requires samples with flat surfaces; hence the use of the cube magnets. To avoid remagnetizing the magnet in the process, the field applied during the measurement was ±0.5 kA/m. The spherical magnets were then assumed to have sustained the same loss in magnetization.
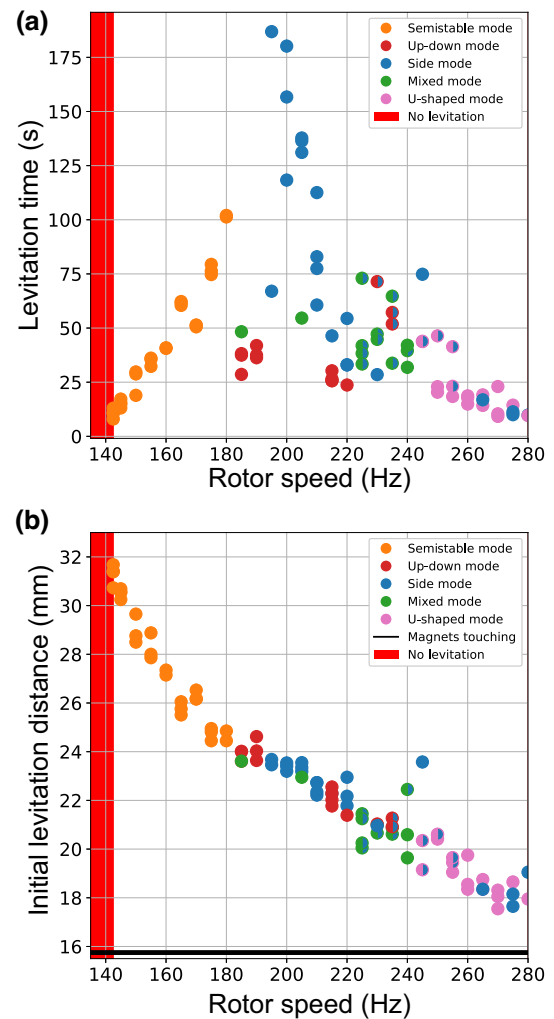

FIG. 3. (a) The levitation time as a function of the rotor speed and (b) the initial levitation distance as a function of the rotor speed. For both figures, the color of the dots denotes the mode occurring during levitation. The multicolored dots mean that the mode changes from the left colored mode to the right colored mode, e.g., for the red-blue case, the mode changes from an up-down mode exclusively to a side mode exclusively. The levitation distance is defined as the distance from the center of the spherical magnet of the rotor to the center of the spherical magnet of the floater.

We first considered the minimum rotor speed needed to achieve levitation. Here, levitation is defined as the floater magnet levitating for more than 0.5 s. The minimum rotor speed as a function of both the floater diameter and the remanence of the floater magnet is shown in Fig. 5(a). To determine the minimum rotor speed, the speed of the rotor was decreased from 400 Hz in steps of 2.5 Hz for the variation in the diameter of the floater magnet and in steps of 1 Hz for the remanence variation. The data points shown in the figure are the lowest rotor speed at which levitation was possible. As can be seen, the magnetization did not influence the minimum rotor speed, as decreasing
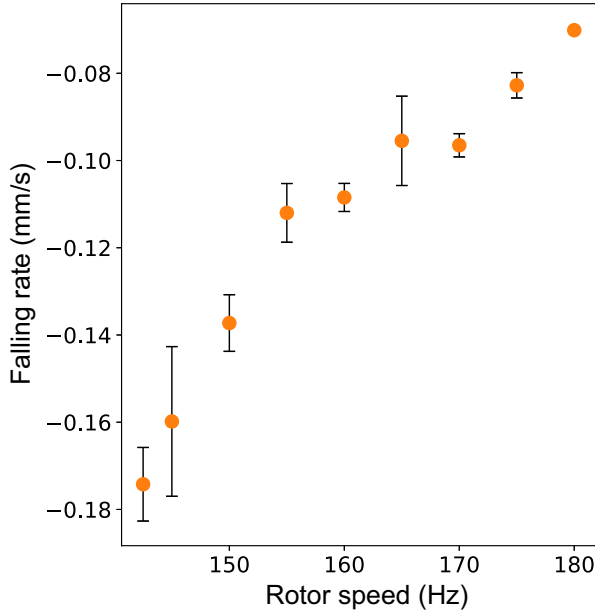
FIG. 4. The fall rate of the floater magnet as a function of the motor speed for the semistable region. The error bars are the standard deviation of three experiments for each rotor speed.

the magnetization by a third from 1180 mT to 760 mT only reduced the minimum rotor speed minimally. However, the sphere size has a very clear influence: the smaller the floater magnet, the higher is the rotor speed necessary to achieve levitation. Thus, this makes it clear that the volume of the floater is important in the dynamics, most likely because inertial effects are playing a dominant part in levitation, although other size effects such as eddy currents could potentially also be present.

We also considered the initial levitation distance as a function of both the diameter of the floater-magnet spheres and the remanence of the floater magnet. This is shown in Fig. 5(b). As can be seen from the figure, an increased remanence resulted in a slightly increased levitation distance. On the contrary, increasing the size of the floater magnet resulted in a shorter levitation distance. This again hints at the interplay between inertial effects and (electro)magnetic forces. Note that the experiments were not done at the same rotor speed, as the variation of the diameter of the floater magnet needs to be done at high rotor speeds to enable all tested spherical magnets to levitate.

D. Discussion

In all measurements presented above, the levitation was limited in time. However, if an aluminum plate is left below the floater, to dampen its oscillation modes by eddy-current dampening, levitation will occur perpetually. In the Supplemental Material [18], the position of a 12.7-mm floater with an aluminum plate 33.5 mm below the center of the rotor magnet and a rotation rate of 240 Hz is shown.

Initially, the floater magnet falls at a rate of 0.3 mm/s for the first 20 s, after which it reaches an equilibrium height, where it levitates for 40 min without any signs of stopping.

Additional experiments were done to explore the nature of the levitation phenomenon. First, it was verified that if a soft-magnetic steel sphere was used as floater, it could not be made to levitate. This was verified for steel spheres of diameters 8, 10, 12.7, and 20 mm and for rotor speeds in the range 50–400 Hz. Regardless of the size and the rotor speeds, the steel sphere was always attracted to the rotor magnet; i.e., there was no repulsion force in the system.

We also performed an experiment in which the floating magnet was an epoxy-bonded cylindrical-shaped magnet with 77.5 vol% Nd-Fe-B magnet material. At 200 Hz, this could also be made to levitate.

We wish to note that the magnetic levitation phenomenon does not require a complicated experimental setup to be realized. We have successfully demonstrated the phenomenon using a simple block magnet glued to a bolt mounted to a high-speed Dremel cutting tool, which can then be used to levitate another block magnet. A video of this is shown in Video 1 or at Ref. [5].

IV. THE PHYSICS OF LEVITATION

There are a number of different experimental observations to explain, including but not limited to translational stability, frequency locking of the rotor and floater rotation, and the relative direction of the magnetic moments. Below, we summarize the relevant physical effects in the system and show how it is not any of the known mechanisms of magnetic levitation, but a different mechanism, that can explain the phenomenon at hand. This is further demonstrated in Sec. V.

The magnetic interactions and external B fields of static uniformly magnetized spheres are precisely those of point dipoles at their centers [20,21]. Thus in a dipole magnetic field, the floater magnet experiences the same force and torque as would a point dipole of magnetic moment $\mathbf{m}_f$ at its center. In the quasistatic limit [22], Faraday's law of induction leads to the electric field $\mathbf{E} = -\partial_t \mathbf{A}$, where $\mathbf{A}$ is the vector potential, but except for the fields of induced currents, the magnetic fields are unchanged. Thus, using the well-known formulas for magnetic point dipoles [21], the fields from the rotor are

$$\mathbf{B}_r = \frac{\mu_0}{4\pi r'^3}\left[3(\hat{\mathbf{r}}' \cdot \mathbf{m}_r)\hat{\mathbf{r}}' - \mathbf{m}_r\right],$$

$$\mathbf{E}_r = \frac{\mu_0}{4\pi}\frac{\hat{\mathbf{r}}' \times \dot{\mathbf{m}}_r}{r'^2},$$

$$(1)$$

where $\mathbf{m}_r$ is the magnetic moment of the rotor, $\mathbf{r}'$ is the position relative to the rotor center, and μ_0 is the vacuum permeability. Also, $\mathbf{r}' = \mathbf{r} - \mathbf{d}$, where $\mathbf{r}$ is position relative to the floater center and $\mathbf{d}$ is the displacement vector
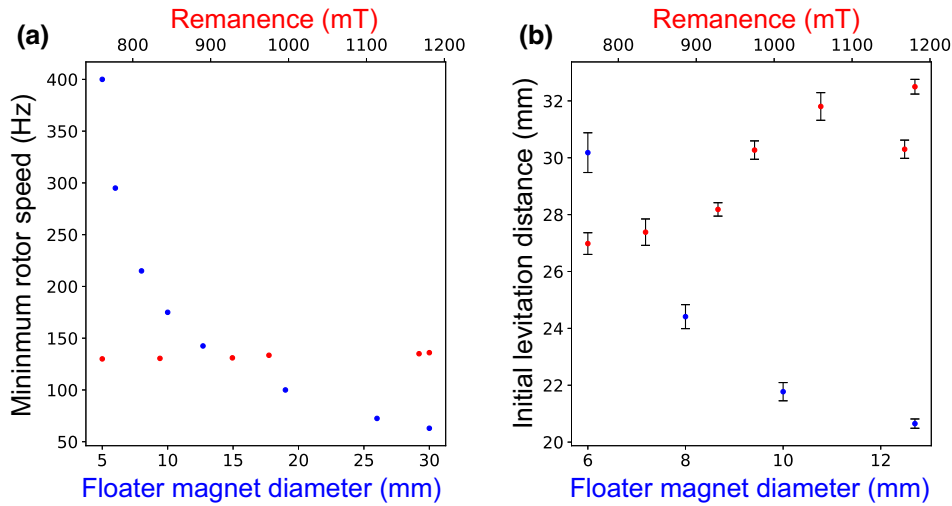
FIG. 5. (a) The minimum rotation speed to achieve levitation as a function of the diameter of the floater-magnet spheres (blue points, bottom x axis) and remanence (red points, top x axis). (b) The initial levitation distance as a function of the diameter of the floater-magnet spheres (blue points, bottom x axis) and remanence (red points, top x axis) at a rotor speed of 150 Hz for the remanence variation and 300 Hz for the variation of the floater-magnet diameter. The error bars given on (b) are the standard deviation of the position as determined by the TRACKER software.

from floater to rotor. We use a hat symbol ("ˆ") to denote normalized vectors and a dot ("˙") for time derivatives.

The magnetic field leads to a dipole torque on the floater [20], $\boldsymbol{\tau}_{\text{dip}} = \mathbf{m}_f \times \mathbf{B}_r(\mathbf{r} = 0)$, which on its own would make $\mathbf{m}_r$ and $\mathbf{m}_f$ antialign, as this is the magnetostatic energy minimum when the positions are fixed. Antialignment is in direct contradiction with observation, so to explain the phenomenon, we require an opposing torque or dynamical effect to stabilize the observed moment configuration.

Clearly, superconduction and feedback stabilization are absent. The only nonelectromagnetic couplings between the floater and the surrounding world are gravity, which does not exert a torque, and fluid effects such as centrifugal suction and air resistance, which either produce zero net torque or exert a drag torque on the floater that is opposite to $\boldsymbol{\omega}_f$ [23–25]. This leaves electrodynamic effects, of which eddy-current drag is the most significant, and gyroscopic effects. We discuss these in Secs. IV A and IV B. It is well established that dissipative and gyroscopic torques can induce steady-state configurations that are energetically unfavorable [26,27] and this is indeed what we observe numerically, as will be discussed subsequently in Sec. V.

A hypothesis proposed by Ucar [4] is that due to a slight out-of-plane rotation of the rotor magnetization $\mathbf{m}_r$ or a shift of the rotor magnet relative to the rotation axis of its holder, $\mathbf{B}_r$ always has a vertical component—say, $B_{r,z}$—at the floater center. Since $B_{r,z}$ is constant, while the horizontal field $\mathbf{B}_{r,\perp}$ rotates rapidly, the former may have a greater impact on the floater dynamics than the small value of $B_{r,z}/B_{r,\perp}$ suggests. Ucar explains vertical stability by a

repulsive force between the horizontal components of $\mathbf{m}_f$ and $\mathbf{B}_r$ countering an attractive force between the vertical components.

We propose that $B_{r,z}$ also dynamically stabilizes the observed moment configuration. In Sec. V, we validate this assumption by reproducing the steady-state levitation and a number of experimental trends, using only magnetostatic dipole interactions and viscous drag. The drag coefficient required to reach the levitating state from rest is orders of magnitude greater than what can be explained by air resistance, suggesting that eddy currents or other electrodynamic loss channels are important.

A. Electrodynamics

In the Supplemental Material [18], we discuss electrodynamic effects in detail. The main takeaway is that the only potentially significant couplings, in addition to those of magnetostatic interactions between rotor and floater, are between the magnetic moments and induced eddy currents. Building on the existing literature [28–38], we derive (cf. the Supplemental Material [18]) an analytical model for the coupling between the rotor moment and eddy currents in the conductive floater and find the torque from eddy currents to be

$$\boldsymbol{\tau}_{\text{eddy}} = \frac{2\pi}{15} \sigma (\omega_r - \omega_f) B_0^2 R_f^5 \hat{\mathbf{z}}. \quad (2)$$

Here, σ is the conductivity, R_f the floater radius, and

$$B_0 = \frac{\mu_0}{4\pi d^3} m_r.$$

In deriving Eq. (2), we have assumed that the rotor is directly above the floater ($\mathbf{d} = d\hat{\mathbf{z}}$) and that both magnets only rotate around the vertical ($\hat{\boldsymbol{\omega}}_r = \hat{\boldsymbol{\omega}}_f = \hat{\mathbf{z}}$), which does not capture the full range of motion. Also, we expand the rotor fields Eq. (1) in R_f/d and only consider the leading order torque, which is equivalent to approximating B_r as uniform. This is not justified, so Eq. (2) should not be regarded as a general solution. That said, it should yield reasonable order-of-magnitude estimates and scaling relations.

If the rotor magnet is conductive, then the floater moment exerts a torque of the same form on the rotor. By angular-momentum conservation, this leads to an equal and opposite torque on the floater. Thus eddy-current coupling of the form in Eq. (2) is present when *either* floater or rotor is magnetic and the other is conductive. Additionally, as the spinning floater induces eddy currents in the environment, it experiences further damping, which can easily exceed the air resistance. We have observed experimentally that increasing this damping using an aluminum block qualitatively changes the dynamics. We note that, in general, coupling of the rotor-moment precession to the floater rotation, as in Eq. 2, is distinct from coupling of the floater-moment precession to rotor rotation. However, this subtlety is irrelevant for the subsequent argument. For the state of motion considered here, the precession of the moments and the rotation of the bulk magnets is at the same frequency, while this is not necessarily the case in our simulations (cf. Sec. V B).

In the absence of all other torques, the equation of motion is $I_f \dot{\boldsymbol{\omega}}_f = \boldsymbol{\tau}_{\text{eddy}}$, where I_f is the floater moment of inertia, in which case the difference in rotation frequency of the floater decays exponentially to the precession frequency of the rotor. This is the phenomenon of frequency locking by eddy-current coupling. Using $I_f = \frac{8}{15}\pi\rho_f R_f^5$, where ρ_f is the mass density of the floater, the exponential time constant can be written as $t_{\text{eddy}} = 4\rho_f/(\sigma B_0^2)$. At a relatively small levitation distance of $d = 20$ mm and the experimentally relevant parameters $\mu_0 M_r = 1.2$ T, $R_r = 9.5$ mm, $\rho_f = 7.5$ g/cm^3 and $\sigma = 667$ Ω^{-1} mm^{-1}, we find $t_{\text{eddy}} = 25$ s, while the experimentally observed frequency locking happens in fractions of a second. For comparison, if we consider only the dipolar torque, then $I_f \dot{\boldsymbol{\omega}}_f = \boldsymbol{\tau}_{\text{dip}} = \mathbf{m}_f \times \mathbf{B}_0$ and, by dimensional analysis, we find the characteristic time $t_{\text{dip}} = \sqrt{I_f/(m_f B_0)}$, which for the same parameter values and $R_f = 6.35$ mm yields 1.7 ms. Thus, the frequency locking in our experiments must be driven by magnetostatic torques rather than eddy currents. We support this hypothesis in Sec. V by numerical experiments.

In deriving Eq. (2), we have made several simplifying assumptions on the floater motion, so in reality $\boldsymbol{\tau}_{\text{eddy}}$ may have a horizontal component. This begs the question if $\boldsymbol{\tau}_{\text{eddy}}$ might stabilize the moment orientation. Since $\mathbf{m}_f$ is

nearly vertical, $\tau_{\text{dip}} \approx m_f B_0$, so in our experiments

$$\frac{\tau_{\text{eddy}}}{\tau_{\text{dip}}} \approx \frac{1}{30}\sigma(\omega_r - \omega_f)R_f^2\left(\frac{R_f}{d}\right)^3\frac{m_r}{m_f} \leq 0.004.$$

This suggests that eddy-current effects are too small to balance the magnetostatic torque. If R_f was an order of magnitude larger, τ_{eddy} could be significant but then self-induction and finite skin depth would also be important, necessitating a more complete analysis.

In summary, no electrodynamic effects can explain the moment orientation on their own. While including the nonuniformity of the rotor field would yield a more correct eddy-current model, we doubt that it would change this conclusion. Instead, we propose that the moment configuration is produced by a vertical field component from imperfections in rotor placement, in conjunction with gyroscopic stabilization.

B. Gyroscopic stability

For a floater with an anisotropic mass distribution, I_f would be a 3×3 tensor and there would be an effective gyroscopic torque of the form [39] $\boldsymbol{\tau}_{\text{gyro}} = -\boldsymbol{\omega}_f \times [I_f \boldsymbol{\omega}_f]$. This complication was absent in our experiments, since we used spheres of uniform density. One thing that does break the spherical symmetry is the intrinsic angular momentum associated with the magnetic moment of the floater. This gyromagnetic effect has been shown in theory to enable the stable levitation of a nanomagnet, even with a static applied field [40,41]; however, as shown in the Supplemental Material [18], the effect was negligibly small for the experiments described in this work.

Thus in the laboratory frame, no gyroscopic terms appear in the rotational equation of motion. That is not to say that gyroscopic stability is absent; in fact, in the rest frame of the rotor magnet, where its magnetic field is constant, there is the fictitious torque $\boldsymbol{\tau}_{\text{fic}} = -I_f \boldsymbol{\omega}_r \times \boldsymbol{\omega}_f$, which bears a strong resemblance to $\boldsymbol{\tau}_{\text{gyro}}$. The cancellation of such a gyroscopic torque with gravity explains why a precessing top remains upright only when spinning rapidly [39]. Equivalently, in the laboratory frame, a certain angular acceleration is required to keep the top rotating and gravity supplies this acceleration instead of making the top fall over. Similarly, for the Levitron, an initial spin around its magnetic moment is required to circumvent Earnshaw's theorem and enable stable levitation [42–44]. In both cases, the argument also works for a spinning sphere.

For our experiments, there is no initial rotation, unlike the Levitron. Nevertheless, in our simulations, the steady-state rotation during levitation is a combination of precession around the vertical and spinning around the magnetic moment, in complete analogy to the spinning top. This state of rotation is gyroscopically stabilized against

changes in the polar angle θ_f. So, in a sense, the rotation itself counteracts the magnetostatic torque. This is further discussed in Sec. V B.

V. SIMULATIONS

A. Model

The motion of the rotor is fully constrained to a predefined trajectory. We model the corresponding time evolution of the floater magnet using the following differential system:

$$I_f \, \dot{\boldsymbol{\omega}}_f = \mathbf{m}_f \times \mathbf{B}_r - \zeta_{\mathrm{rot}} \boldsymbol{\omega}_f, \tag{3}$$

$$\mathfrak{m}_f \, \dot{\mathbf{v}}_f = \mathbf{F}_{\mathrm{dip}} - \zeta_{\mathrm{trans}} \mathbf{v}_f - g\hat{\mathbf{z}}, \tag{4}$$

where $g = 9.82$ m/s^2 is the gravitational acceleration, $\mathbf{v}_f$ is the floater velocity, $\mathbf{B}_r$ is the rotor field from Eq. (1) evaluated at the center of the floater, and

$$\mathbf{F}_i^{\mathrm{dip}} = \frac{3\mu_0}{4\pi} \frac{1}{r_{rf}^4} [(\mathbf{m}_f \cdot \hat{\mathbf{r}}_{rf})\mathbf{m}_r + (\mathbf{m}_r \cdot \hat{\mathbf{r}}_{rf})\mathbf{m}_f$$
$$+ (\mathbf{m}_f \cdot \mathbf{m}_r)\hat{\mathbf{r}}_{rf} - 5(\mathbf{m}_f \cdot \hat{\mathbf{r}}_{rf})(\mathbf{m}_r \cdot \hat{\mathbf{r}}_{rf})\hat{\mathbf{r}}_{rf}] \tag{5}$$

is the dipole force from the rotor on the floater, where $\mathbf{r}_{rf}$ is the displacement from the rotor to the floater. We note that these magnetostatic interactions are exact for uniformly magnetized spheres[20]. For the drag coefficients, we use analytical solutions for viscous drag but with an effective viscosity to model eddy-current damping, i.e.,

$$\zeta_{\mathrm{rot}} = 8\pi \eta_{\mathrm{eff}} R_f^3, \quad \zeta_{\mathrm{trans}} = 6\pi \eta_{\mathrm{eff}} R_f. $$

This drag is exact for an isolated sphere at low Reynolds number [45] and has the same linear dependence on angular velocity as we expect from eddy currents [cf. Eq. (2)]. Unless otherwise stated, we have used an efficient viscosity of $\eta = 1$ Pa · s in the simulations. For reference, the viscosity of air at ambient conditions is $\eta_{\mathrm{air}} = 0.02$ mPa · s, while for water the value is $\eta_{\mathrm{H_2O}} = 1$ mPa · s.

This type of model is well established for magnetic nanoparticles, i.e., nanoscale magnetized spheres suspended in liquid [46]. That said, the eddy-current damping depends strongly on the floater position, yielding more complex instabilities and transient behavior, so we can at best reproduce qualitative trends and observations with the present model. The fact that the model does produce levitation suggests that the phenomenon could also be achieved for entirely nonconducting magnets by means other than eddy-current damping. The increased drag can be made possible by submerging the floater in viscous liquid.

One feature specific to the present model is related to the angular velocity around the magnetic moment, i.e., $\omega_m =$

$\hat{\mathbf{m}}_f \cdot \boldsymbol{\omega}_f$. From Eq. (3), we have

$$\dot{\omega}_m = [\boldsymbol{\omega}_f \times \hat{\mathbf{m}}_f] \cdot \boldsymbol{\omega}_f + \frac{1}{I_f} \hat{\mathbf{m}}_f \cdot [\mathbf{m}_f \times \mathbf{B}_r - \zeta_{\mathrm{rot}} \boldsymbol{\omega}_f]$$

$$= -\frac{\zeta_{\mathrm{rot}}}{I_f} \omega_m.$$

That is, ω_m can only decrease exponentially, so when it starts at zero, $\omega_m = 0$ at all times. We have verified this numerically for all simulations. In general, this is not true with eddy-current coupling.

To simulate Eqs. (3) and (4), we use velocity-Verlet time-step integration with a time step of 1 μs [47]. To rotate $\mathbf{m}_f$, we use the Euler-Rodrigues rotation formula [48].

B. Results: Fixed floater position

We find that for most parameters, the simulated floater will either fall under gravity or collide with the rotor and be flung away. Therefore as a first study, we keep the center position of the floater fixed and only consider the rotational motion.

For all simulations, the floater is initially at rest and centered on the rotation axis, which is vertical. We find that the steady state is not sensitive to the initial orientation, so we only use $60°$ from the vertical in the *x-z* plane, i.e., $\hat{\mathbf{m}}_f(t=0) = (\sin(60°), 0°, \cos(60°))$. The rotor configuration is given by

$$\mathbf{r}_r = \begin{pmatrix} \delta_r \cos(2\pi f_r t) \\ -\delta_r \sin(2\pi f_r t) \\ d \end{pmatrix}, \quad \mathbf{m}_r = \begin{pmatrix} \cos(\varphi_0 - 2\pi f_r t) \\ \sin(\varphi_0 - 2\pi f_r t) \\ 0 \end{pmatrix}. \tag{6}$$

That is, the rotor magnet is a distance d vertically above the floater, except for a small lateral shift of δ_r away from the rotation axis. Its holder rotates clockwise at frequency f_r with the moment in the *x-y* plane and pointing away from the rotation axis. We use $\varphi_0 = 60°$ as the initial condition. We distinguish between distance r_{rf} and vertical distance d but since $\delta_r \ll d$, they are nearly equal. Besides the lateral shift, the setup is identical to Fig. 2.

With the floater centered on the rotation axis, the only effect of δ_r is to produce a constant vertical B field. Since $\mathbf{m}_r$ points away from the rotation axis, $B_{r,z} > 0$, while if $\mathbf{m}_r$ pointed toward the axis, we would have $B_{r,z} < 0$. The same effect can be achieved by giving $\mathbf{m}_r$ an out-of-plane tilt. We have verified that for either sign, $m_{f,z}$ points in the field direction.

Without a vertical field, the steady state always has $\mathbf{m}_f$ in the *x-y* plane, corresponding to a polar angle of $\theta_f = 90°$. While $\delta_r = 1$ mm seems small, for some frequencies the resulting $B_{r,z}$ is sufficient to make $\mathbf{m}_f$ nearly vertical. We find that depending on the system parameters, there

are three different dynamical phases with radically different steady-state behavior and sharp transitions in parameter space.

In Fig. 6, we present simulation data for a range of different frequencies and distances. Figures 6(a)–6(c) illustrate the three ("red," "green," and "blue") dynamical phases. Figure 6(a) shows that at low and high f_r, the phase angle is essentially constant, with a value close to either $180°$ or $0°$ (red and blue curves, respectively), i.e., the rotor and floater are frequency locked. At intermediate frequencies, $\mathbf{m}_f$ rotates more slowly than $\mathbf{m}_r$ but there is a secondary precession at equal frequency; hence the fast oscillations on the green curves in Figs. 6(b) and 6(c). We note that when increasing f_r or d, the time-averaged value of θ_f decreases gradually from $90°$ to $0°$.

In Fig. 6(d), we see the distribution of dynamical phases in parameter space. Each data point corresponds to a 5-s simulation, where we have computed the average and standard deviation of φ over the last 250 ms. The green points have standard deviations above $1°$, while the blue and red points have standard deviations below $1°$. Except for a few points on the phase boundaries, the standard deviation is either above $50°$ or less than 10^{-6}, i.e., there is a sharp contrast, so the phase determination for a given simulation is unambiguous. To distinguish blue and red, we use the steady-state value of φ. In the Supplemental Material [18], we show similar plots where we have varied η, R_f, M_f, or δ_r instead of f_r.

The red phase is the energy minimum, which would be the final configuration with a static rotor, i.e., when $f_r = 0$. Thus it makes sense that the red phase occurs at the lowest frequencies and at shorter distances, where the energy minimum is lowest. At intermediate frequencies and distances, inertia and drag mean that the floater cannot keep up, so while there is a net clockwise rotation, it is only the smaller secondary precession that follows the rotor frequency. As the frequency increases, the floater is less and less susceptible to the rotating horizontal field but still responds to the constant vertical field; hence $\mathbf{m}_f$ becomes increasingly vertical. When θ_f is near zero, the secondary precession disappears and frequency locking is reestablished, i.e., the green phase transitions to blue.

To explain why the blue phase occurs, we first infer an expression for the angular velocity. We know that $\dot{\varphi} = 0$, so there is a clockwise precession around the vertical at a frequency of ω_r. Also, $\dot{\theta}_f = 0$, so the only possible form of rotation is spinning around $\mathbf{m}_f$. That is, $\boldsymbol{\omega}_f = -\omega_r \hat{\mathbf{z}} + \dot{\psi} \hat{\mathbf{m}}$. Using that $\mathbf{m}_f \cdot \boldsymbol{\omega}_f = 0$, as discussed in Sec. V A, we find that $\dot{\psi} = \omega_r \cos \theta_f$; hence the angular velocity is

$$\boldsymbol{\omega}_f = \omega_r[-\hat{\mathbf{z}} + \cos \theta_f \, \hat{\mathbf{m}}] \quad \text{(blue phase).} \quad (7)$$

We have verified that each component fits the simulations to within a relative error of 0.0004% throughout the blue phase. The magnitude is simply $\omega_f = \omega_r \sin \theta_f$.

Counterintuitively, the floater spins around its moment precisely because the *net* angular velocity around $\mathbf{m}_f$ must be zero and there is a contribution from the precession of $\mathbf{m}_f$ around the vertical. This spinning gyroscopically stabilizes against changes in θ_f, analogously to how a spinning top defies gravity [39]. Equivalently, in the rest frame of the rotor, the spinning yields a fictitious gyroscopic torque that balances the magnetostatic torque. When $\mathbf{m}_f$ is close to the vertical, the angular-velocity vectors from precession and from spinning around $\mathbf{m}_f$ nearly cancel, so that the magnitude of ω_f is tiny. Consequently, the drag torque is small and does not hinder frequency locking.

By inserting Eq. 7 in the governing equation Eq. 3, we obtain a set of equations that θ_f and φ must obey for self-consistency. In the Supplemental Material [18], we expand said equations to leading order in the small angles θ_f, φ and isolate, which yields

$$\varphi = \frac{\zeta_{\text{rot}}\omega_r}{I_f \omega_r^2 - m_f B_{r,z}} \quad \text{and} \quad \theta_f = \frac{m_f B_{r,\perp}}{I_f \omega_r^2 - m_f B_{r,z}}. \quad (8)$$

Comparing with the blue simulations in Fig. 6(d), the greatest relative error is 1.8% for φ and 0.05% for θ_f, so higher-order corrections are more significant for φ. From Eq. 8, we see that a finite moment of inertia is required for the blue phase to occur, because a negative value of θ_f is unphysical, but drag is not required for self-consistency. $I_f \sim R_f^5$, so the importance of inertia may explain why the critical frequency has a strong size dependence despite a weak dependence on magnetization, as seen in Fig. 5(a) and the Supplemental Material [18].

The next question is how the computed rotational states can produce stable levitation. In the red phase, the magnets are consistently attractive. In the green phase, the force oscillates at a frequency of f_r but it averages to a net repulsion—at least, for all the parameter combinations that we have simulated. While this repulsion could balance gravity in special cases, our experiments have shown stability regardless of whether the floater was above or below the rotor, so this would be a different form of levitation. That leaves the blue phase, where φ, θ_f, and the vertical force F_z are all constant.

In Fig. 6(f), we show the vertical force for frequencies from 270 to 360 Hz. It is apparent that the force curves are nonmonotonous. This is because the magnetic force changes from attractive ($F_z > 0$) to repulsive ($F_z < 0$) with decreasing distance. Every point at which F_z crosses zero from positive to negative as d decreases is a stable equilibrium, because a slight displacement in either direction leads to a restoring force. In some cases, the maximum attractive force is less than gravity; in others, the magnets would collide before reaching the stable point. In Fig. 6, we have marked all midair stable points by orange crosses. We note that the levitation distance decreases with increasing frequency, in agreement with Fig. 3.
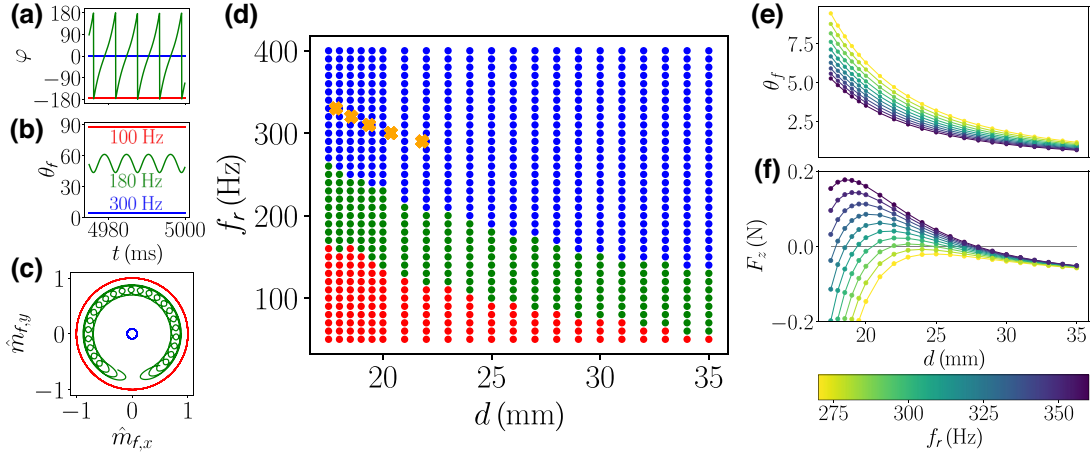
FIG. 6. The simulation results at various rotor frequencies with the floater position fixed. The rotor is displaced by $\delta_r = 1$ mm relative to the rotation axis, yielding a slight vertical B field, the effective damping is $\eta = 1$ Pa · s, both magnetizations are 1.18 T, and the diameters are 12.7 and 19 mm for the floater and rotor, respectively. (a)–(c) The steady-state behavior in the three different dynamical phases for $d = 20$ mm: (a),(b) the phase lag, φ, and floater polar angle, θ_f, versus time over 25 ms; (c) the transverse components of the normalized floater moment over 150 ms. (d) The dynamical phase of every simulation at various rotor frequencies, f_r, and rotor and/or floater distances d. The orange crosses mark stable force equilibria. (e),(f) θ_f and the vertical force F_z for all simulations in the blue phase between 270 and 360 Hz. The stable equilibria are the points where spline fits of the force curves in (f) cross from positive (attractive) to negative (repulsive) as d decreases.

To understand the force curves, we note that the blue phase is close to the configuration $\theta_f = \varphi = 0°$ and $\delta_r/d \ll 1$. Therefore, we consider a Taylor expansion of the dipole force [Eq. (5)] in these three variables. To zeroth order, $\hat{\mathbf{m}}_f = \hat{\mathbf{r}}_{rf} = \hat{\mathbf{z}}$, which is perpendicular to $\mathbf{m}_r$, in which case the vertical force is zero. To first order,

$$F_{\mathrm{dip},z} \approx \frac{3\mu_0 m_r m_f}{4\pi d^4}\left[4\frac{\delta_r}{d} - \theta_f\right] \quad \text{(blue phase)}.$$

The first term is an attractive force between the vertical components of $\mathbf{B}_r$ and $\mathbf{m}_f$. The second term is a repulsion between horizontal components. From Fig. 6(e), we see that θ_f increases with decreasing distance and that the relative change is greater than that in δ_r/d. This is why $F_{\mathrm{dip},z}$ can change from attractive to repulsive in midair. In other words, as the magnets approach, the floater moment becomes more horizontal, which makes the repulsive dipole force grow *relative to* the attractive dipole force. This explanation is in agreement with Ref. [4].

C. Results: Free floater position

Here, the rotor is fully constrained as in Eq. (6), while the floater is free to both rotate and translate in 3D space. We find that with the right parameters, the model [Eqs. (3) and (4)] does produce stable levitation. In Video 10 is shown an example simulation at $f_r = 300$ Hz and with the same parameters as Fig. 6, except that $\delta_r = 1.2$ mm. We have been unable to produce levitation at $\delta_r = 1$ mm, which we attribute to the translational motion making frequency locking less stable. For the same reason, the

steady-state vertical distance of $d = 22.5$ mm is slightly higher than expected from Fig. 6(d), i.e., from the orange cross at 300 Hz.

We observe from Videos 10(a) and 10(b) that we obtain the expected dynamical phase and from Videos 10(c) and 10(d) that the levitation is stable in all directions. In the steady state, the floater z coordinate and the relative orientation of the magnets settle to constants, while the x and y coordinates of the floater perform sinusoidal oscillations, just like the side mode observed experimentally [see the inset in Video 10(d)]. Note how all of the configurational variables reach steady state within 0.5 s, which is much faster than frequency locking by eddy currents (cf. Sec. IV A).

We have obtained qualitatively identical results when generating the vertical B field by giving $\mathbf{m}_r$ a 5° out-of-plane tilt, rather than a lateral shift of the whole magnet. This is nontrivial, as $\mathbf{B}_r$ scales differently with the floater position for the two imperfections in rotor placement. Indeed, Ucar has found experimentally that levitation also occurs when the constant field is from a third stationary dipole magnet [4, Fig. 20]. We conclude that the key aspect that enables this novel form of magnetic levitation is the superposition of stationary and time-varying magnetic fields, not the specific rotor perturbations.

When letting the system relax at $\eta = 1$ Pa · s for 1 s and then turning off all damping, the final configuration remains stable indefinitely. It still exhibits the side mode. This shows that damping is not strictly required to sustain the moment orientation that yields levitation. Rather,
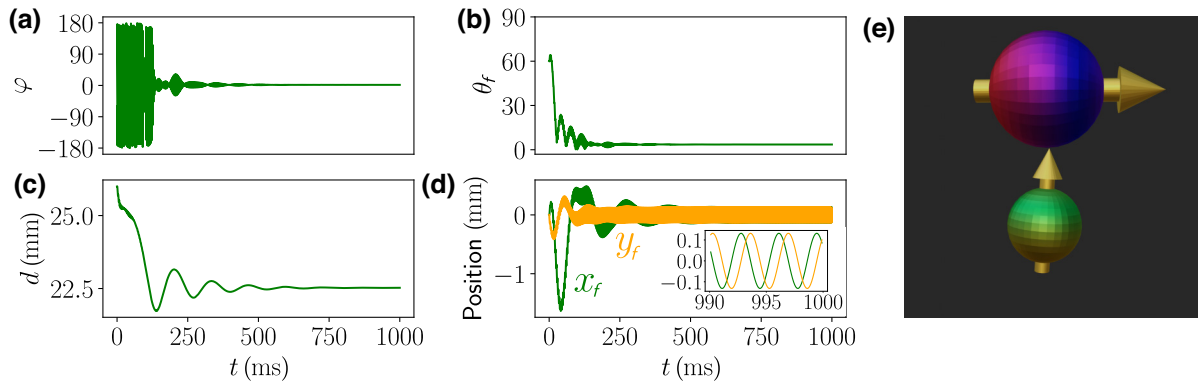
VIDEO 10.   Simulated levitation at a rotor frequency of $f_r = 300$ Hz, where the floater has full rotational and translational freedom. The parameters are the same as in Fig. 6 except that $\delta_r = 1.2$ mm. (a) The phase angle. (b) The floater polar angle. (c) The vertical floater or rotor distance. (d) The x, y position of the floater, with the origin on the rotation axis of the rotor. The inset in (d) shows the last 10 ms of the 1-s simulation. (e) The final configuration. The blue-red sphere is the rotor, the green-orange sphere is the floater, and the yellow arrows represent magnetic moments. The positions and sizes are to scale.

damping serves to facilitate reaching the levitating state from rest and to increase the stability thereof.

D. Comparison of simulations and experiments

In Secs. V A, V B, and V C, we have shown that a model including only magnetostatic (dipole) coupling and damping can reproduce stable levitation in certain parameter ranges. The effect of gravity is to shift the point of stability but it alters none of the qualitative features. The model has no features that are unique to eddy currents, as the same damping can be achieved by putting the floater in liquid, and while moderate viscous damping facilitates levitation, it is not a strict requirement.

This suggests that the levitation effect is quite general and since dipole interactions are significant across many length scales, it should be scalable. The relatively small moment of inertia might be an issue for the levitation of microparticles but perhaps this can be compensated by increasing the frequency of the rotating field.

The simulations are qualitatively consistent with the experiments in terms of how the levitation distance scales with the rotor speed [cf. Figs. 3(b) and 6(d)] and with the floater size [see Fig. 5(b) and the Supplemental Material [18]]. These are strong indications that the model contains most of the essential physics.

Quantitatively, the simulations have room for improvement. From the orange crosses in Fig. 6(d), we see that levitation is predicted at higher frequencies and a narrower frequency band than found experimentally [see Fig. 3(b)]. Also, while Video 10(d) is consistent with the side mode in Video 7, we have not observed any vertical oscillations in the steady state, so our simulations do not reproduce the up-down, U-shaped, or mixed mode. Regarding the semistable mode, when our simulations reach steady

state, the system remains stable indefinitely, even without damping.

Experimentally, we have observed indefinite stability when an aluminum block was placed below the floater, which has the effect of increasing damping. So our numerical model is perhaps more representative of this setup. While the point of stability shown in Video 10 is largely consistent with Fig. 6(d), the floater orientation and force curve will change at least slightly when including floater translation. In addition, the system is highly sensitive to the constant B field, so quantitative experimental comparison requires a more accurate determination of the trajectory of the rotor magnet, i.e., δ_r and θ_r. Alternatively, one can use a stationary third magnet to generate the constant field.

On the modeling side, we believe that the main point of improvement is the drag. At $f_r = 200$ Hz, we find that a viscosity of at least 0.01 Pa · s is required to produce the blue phase from rest (see the Supplemental Material [18]), which cannot be explained by air resistance. If, as we suspect, the main source of damping is eddy currents, then this has a number of implications. The relative magnitude of translational and rotational damping in Video 10 is most likely incorrect; Eq. (2) suggests a stronger dependence on floater size and magnetization than the simulated model and damping would be a function of position. Finally, there is a distinction between eddy-current *damping* from the stationary environment, and eddy-current *coupling* between the two rotating magnets, which can also accelerate the floater.

A more accurate model of damping, both rotational and translational, may be required to explain the relatively complex set of translational modes or the gradual change in the equilibrium distance observed in the semistable mode. In particular, we note that our explanation for the stability of the moment orientation relies heavily on the angular-velocity component $\omega_m = \hat{\mathbf{m}} \cdot \boldsymbol{\omega}_f$ being constantly zero.

We hypothesize that the breaking of this conservation law by eddy-current coupling is related to the very gradual decrease in levitation height over time recorded in Fig. 4 but further investigation is required.

VI. CONCLUSIONS

We have demonstrated that magnetic levitation of a permanent magnet can be achieved by placing it in the vicinity of another magnet rotating at angular velocities in the order of 200 Hz. Rotating a 19-mm-diameter spherical Nd-Fe-B magnet, the levitation phenomenon has been demonstrated for spherical Nd-Fe-B magnets in the (5–30)-mm-diameter range. First, we have shown experimentally that the floating magnet aligns to the like pole of the rotating magnet, i.e., opposite to what would be expected from magnetostatics. For a floating magnet with a diameter of 12.7 mm, we have measured the polar and azimuthal (phase) angles as $\theta_f = 7° \pm 4°$ and $\varphi = 6.4° \pm 5.1°$, respectively. Then, we have investigated the instabilities occurring during levitation and observed five different patterns of motion. Afterward, we have assessed the influence of the rotation speed, as well as the size and magnetization of the floating magnet, on levitation. We have found that the magnetization of the floating magnet does not affect the rotation speed needed for levitation (in the case of remanence fields of 760–1180 mT), while its size has a very clear influence: the smaller the floating magnet, the higher is the rotor speed necessary to achieve levitation and the further the floating magnet levitates from the rotating magnet. Subsequently, we have discussed the underlying physics of the system. A thorough analysis reveals that electrodynamic effects are orders of magnitude too small to sustain the levitating state. However, using a numerical model involving only magnetostatics and eddy-current-enhanced damping, we have reproduced the experimental trends and stable levitation. The key is a constant vertical magnetic field component, which may originate from small imperfections in the positioning of the rotor magnet. This enables the counterintuitive steady-state moment orientation, which is gyroscopically stabilized and in turn gives the magnetostatic force a stable midair equilibrium point.

All the data presented in this work, including all video captures, are available from the data repository at Ref. [17]. This includes the videos of all experiments described in the text. The videos can also be found at Ref. [5].

[1] H.-W. Lee, K.-C. Kim, and J. Lee, Review of Maglev train technologies, IEEE Trans. Magn. **42,** 1917 (2006).

[2] D. K. Supreeth, S. I. Bekinal, S. Rokkad Chandranna, and M. Doddamani, A review of superconducting magnetic bearings and their application, IEEE Trans. Appl. Supercond. **32,** 1 (2022).

[3] J. de Boeij, E. Lomonova, and J. Duarte, Contactless planar actuator with manipulator: A motion system without cables and physical contact between the mover and the fixed world, IEEE Trans. Ind. Appl. **45,** 1930 (2009).

[4] H. Ucar, Polarity free magnetic repulsion and magnetic bound state, Symmetry **13,** 442 (2021).

[5] R. Bjørk, J. M. Hermansen, and F. L. Durhuus, Youtube channel "Magnetic levitation," https://youtube.com/playlist?list=PLOfbFSFa_WoK4PgYQXhuNucS_WcIxXDET (2023).

[6] J. W. Jansen, C. M. M. van Lierop, E. A. Lomonova, and A. J. A. Vandenput, Magnetically levitated planar actuator with moving magnets, IEEE Trans. Ind. Appl. **44,** 1108 (2008).

[7] G. Schweitzer, in *IUTAM Symposium on Emerging Trends in Rotor Dynamics*, edited by K. Gupta, IUTAM Bookseries Vol. 1011 (Springer Netherlands, Dordrecht, 2011), p. 263.

[8] M. M. Michaelis and D. B. Taylor, Stability of vertical and horizontal axis Levitrons, Eur. J. Phys. **36,** 065003 (2015).

[9] M. M. Michaelis, Horizontal axis Levitron—a physics demonstration, Phys. Educ. **49,** 67 (2014).

[10] M. Perdriat, C. Pellet-Mary, T. Copie, and G. Hétet, Planar magnetic Paul traps for ferromagnetic particles, arXiv:2212.11622 (2022).

[11] C. Sackett, E. Cornell, C. Monroe, and C. Wieman, A magnetic suspension system for atoms and bar magnets, Am. J. Phys. **61,** 304 (1993).

[12] R. F. Gans, T. B. Jones, and M. Washizu, Dynamics of the Levitron^{tm}, J. Phys. D: Appl. Phys. **31,** 671 (1998).

[13] L. N. Pham, G. F. Tabor, A. Pourkand, J. L. B. Aman, T. Hermans, and J. J. Abbott, Dexterous magnetic manipulation of conductive non-magnetic objects, Nature **598,** 439 (2021).

[14] G. F. Tabor, L. N. Pham, J. J. Abbott, and T. Hermans, in *Proceedings of Robotics: Science and Systems* (New York City, NY, USA, 2022).

[15] D. K. Dalton, G. F. Tabor, T. Hermans, and J. J. Abbott, Attracting conductive nonmagnetic objects with rotating magnetic dipole fields, IEEE Robot. Autom. Lett. **7,** 11484 (2022).

[16] H. Ucar, Directional quantization of an oscillatory magnetic dipole moment associated with a moment of inertia (2023), https://doi.org/10.31219/osf.io/pkusx.

[17] J. M. Hermansen and R. Bjørk, Data for magnetic levitation by rotation. *data.dtu.dk* (2023), https://doi.org/10.11583/DTU.22292947.

[18] See the Supplemental Material at http://link.aps.org/supplemental/10.1103/PhysRevApplied.20.044036 for additional experimental details, derivations of the effect of magnetic angular momentum and eddy-current coupling, and additional simulation results.

[19] M. Haavisto, S. Tuominen, T. Santa-Nokki, H. Kankaanpää, M. Paju, and P. Ruuskanen, Magnetic behavior of sintered NdFeB magnets on a long-term timescale, Adv. Mater. Sci. Eng. **2014,** 1 (2014).

[20] B. F. Edwards, D. M. Riffe, J.-Y. Ji, and W. A. Booth, Interactions between uniformly magnetized spheres, Am. J. Phys. **85,** 130 (2017).

[21] D. J. Griffiths, *Introduction to Electrodynamics* (Pearson, Boston, Massachusetts, 2013), 4th ed.

[22] J. Larsson, Electromagnetics from a quasistatic perspective, Am. J. Phys. **75,** 230 (2007).

[23] M. Schuck, D. Steinert, T. Nussbaumer, and J. W. Kolar, Ultrafast rotation of magnetically levitated macroscopic steel spheres, Sci. Adv. **4,** e1701519 (2018).

[24] N. Lukerchenko, Y. Kvurt, I. Keita, Z. Chara, and P. Vlasak, Drag force, drag torque, and magnus force coefficients of rotating spherical particle moving in fluid, Part. Sci. Technol. **30,** 55 (2012).

[25] M. Turkyilmazoglu, Radially expanding/contracting and rotating sphere with suction, Int. J. Numer. Methods Heat Fluid Flow **32,** 3439 (2022).

[26] R. Krechetnikov and J. E. Marsden, Dissipation-induced instabilities in finite dimensions, Rev. Mod. Phys. **79,** 519 (2007).

[27] N. M. Bou-Rabee, J. E. Marsden, and L. A. Romero, Tippe top inversion as a dissipation-induced instability, SIAM J. Appl. Dyn. Syst. **3,** 352 (2004).

[28] H. Hertz, On induction in rotating spheres, Lond. Edinb. Dublin Philos. Mag. J. Sci. **10,** 451 (1880).

[29] T. Reichert, T. Nussbaumer, and J. W. Kolar, Complete analytical solution of electromagnetic field problem of high-speed spinning ball, J. Appl. Phys. **112,** 104901 (2012).

[30] K. T. McDonald, Conducting sphere that rotates in a uniform magnetic field (Joseph Henry Laboratories, Princeton University, Princeton, NJ, 2002).

[31] R. C. Youngquist, M. A. Nurge, S. O. Starr, F. A. Leve, and M. Peck, A slowly rotating hollow sphere in a magnetic field: First steps to de-spin a space object, Am. J. Phys. **84,** 181 (2016).

[32] M. A. Nurge, R. C. Youngquist, R. A. Caracciolo, M. Peck, and F. A. Leve, A thick-walled sphere rotating in a uniform magnetic field: The next step to de-spin a space object, Am. J. Phys. **85,** 596 (2017).

[33] M. A. Nurge, R. C. Youngquist, and S. O. Starr, Drag and lift forces between a rotating conductive sphere and a cylindrical magnet, Am. J. Phys. **86,** 443 (2018).

[34] G. Backus, The external electric field of a rotating magnet, Astrophys. J. **123,** 508 (1956).

[35] P. Lorrain, Electrostatic charges in v*B fields: The Faraday disk and the rotating sphere, Eur. J. Phys. **11,** 94 (1990).

[36] P. Lorrain, J. McTavish, and F. Lorrain, Magnetic fields in moving conductors: Four simple examples, Eur. J. Phys. **19,** 451 (1998).

[37] Y. Yu, H. Yue, F. Yang, H. Zhao, and Y. Lu, Electromagnetic interaction between a slowly rotating conducting shell and magnetic dipoles: A theoretical and numerical study, IEEE Trans. Magn. **57,** 1 (2021).

[38] Y. Yu, H. Yue, H. Zhao, F. Yang, and X. Chen, Optimal configuration of distributed HTS coils for the non-contact de-tumbling of space debris, Acta Astronaut. **191,** 491 (2022).

[39] G. R. Fowles and G. L. Cassiday, *Analytical Mechanics* (Thomson Brooks/Cole, Belmont, California, 2005), 7th ed.

[40] C. C. Rusconi, V. Pöchhacker, K. Kustura, J. I. Cirac, and O. Romero-Isart, Quantum spin stabilized magnetic levitation, Phys. Rev. Lett. **119,** 167202 (2017).

[41] K. Kustura, V. Wachter, A. E. Rubio López, and C. C. Rusconi, Stability of a magnetically levitated nanomagnet in vacuum: Effects of gas and magnetization damping, Phys. Rev. B **105,** 174439 (2022).

[42] M. V. Berry, The Levitron: An adiabatic trap for spins, Proc. R. Soc. London. Ser. A: Math. Phys. Eng. Sci. **452,** 1207 (1996).

[43] M. D. Simon, L. O. Heflinger, and S. L. Ridgway, Spin stabilized magnetic levitation, Am. J. Phys. **65,** 286 (1997).

[44] T. B. Jones, M. Washizu, and R. Gans, Simple theory for the Levitron®, J. Appl. Phys. **82,** 883 (1997).

[45] S. I. Rubinow and J. B. Keller, The transverse force on a spinning sphere moving in a viscous fluid, J. Fluid Mech. **11,** 447 (1961). Publisher: Cambridge University Press.

[46] F. L. Durhuus, L. H. Wandall, M. H. Boisen, M. Kure, M. Beleggia, and C. Frandsen, Simulated clustering dynamics of colloidal magnetic nanoparticles, Nanoscale **13,** 1970 (2021).

[47] P. Young, The leapfrog method and other "symplectic" algorithms for integrating Newton's laws of motion, Lecture notes, University of California, Santa Cruz (2014).

[48] H. Cheng and K. C. Gupta, An historical note on finite rotations, J. Appl. Mech. **56,** 139 (1989).